Appl. Phys. A 79, 1385–1389 (2004)
DOI: 10.1007/s00339-004-2787-7

Applied Physics A
Materials Science & Processing

C.R. PHIPPS[1,✉]
J.R. LUKE[2]
T. LIPPERT[3]
M. HAUER[3]
A. WOKAUN[3]

Micropropulsion using laser ablation

[1] Photonic Associates, 200A Ojo de la Vaca Road, Santa Fe, NM 87508, USA
[2] Institute for Engineering Research and Applications, 901 University Blvd. SE, Albuquerque, NM 87106-4339, USA
[3] Paul Scherrer Institut, 5232 Villigen PSI, Switzerland

Received: 29 September 2003/Accepted: 18 March 2004
Published online: 26 July 2004 •

ABSTRACT The micro-laser plasma thruster (μLPT) is a new micropropulsion device that uses laser ablation to create very small thrusts (0.1–100 μN) for pointing and positioning micro- and nano-satellites. In this paper, we discuss the expected performance of the μLPT. For a ms-pulse device, target materials are restricted to those of low thermal conductivity, e.g. polymers. Volume ablation theory adequately describes their behavior. In a ns-pulse version, exhaust velocity can be an order of magnitude higher with correspondingly lower thrust-to-power ratio. The theory for surface absorbers describes the observed behavior.

PACS 45.55.Px; 42.70.Jk; 52.50.Jm; 42.62.Cf; 42.70.Km; 78.66.Qr

1 Introduction

In earlier work [1–4], we reported the behavior of microthrusters driven by simple laser diodes. Because diodes are essentially constant-power devices with single-device output in the few-watt range, the intersection of diode output capabilities (even with very fast lenses) with the threshold for plasma-jet formation on targets requires us to use ms-duration pulses in this case. For such long pulses, thermal conduction in the target is a dominant heat sink, ruling out many materials, including all metals and even some polymers.

Table 1 compares the demonstrated performance of the ms device with the predicted performance of a ns-pulse thruster. Advantages of ns-pulse operation include the use of metallic targets, use of reflection-mode target-illumination geometry (offering simple target design and maximum target performance), and operation in the fully ionized plasma regime, which will reduce spacecraft contamination. We note that a specific impulse up to 8000 s has been observed [5] at intensities like those in the 'ns-pulse' column of Table 1. Lasers suitable for operation with these parameters have been reported over the past two years [6]. Gonzales and Baker were the first to discuss such a ns-pulse microthruster [7] in the literature.

✉ Fax: +1-505/466-3877, E-mail: crphipps@aol.com

Laser version	ns-pulse	ms-pulse
Pulse duration τ (ns)	1	2×10^6
Average optical power on target P (W)	4	2
Peak optical power on target P_{pk} (kW)	230	0.012
NA of target optics	0.07	0.68
Lens diameter d_L (mm)	20	6
Standoff distance s_2 to target (mm)	150	3
Optics contamination time, R-mode	230 h [b]	20 s [a]
Repetition rate f (kHz)	17	0.080
Pulse energy W (mJ) [c]	0.23	25
Spot size on target (μm)	100	25
Fluence Φ on target (J/cm^2)	2.9	4900
Intensity on target (GW/cm^2)	2.9	0.0028
Specific impulse I_{sp} (s)	10000	500–1000
Momentum coupling coeff. C_m (dyn/W)	2	20–40

[a] at near-normal incidence
[b] at 45° incidence
[c] with laser under development

TABLE 1 Comparison of predicted ns-pulse and demonstrated ms-pulse μLPTs

2 Modeling

In this section, we describe the code we developed to model the ns-duration laser–target interaction, and the theory behind its operation.

2.1 *Vapor regime*

As laser intensity increases, materials first pass through the vapor regime before the fully ionized plasma model [8] applies. For low-intensity pulses, plasma ignition may never be achieved, but still generate significant values of C_m, the ratio of ablation momentum produced to incident pulse energy.

We write a Clausius–Clapeyron equation for the surface pressure:

$$p(\text{atm}) = \frac{p}{p_1} = \exp\left[\frac{H_1}{kT_1} - \frac{H}{kT}\right], \quad (1)$$

where the subscript '1' refers to a one-atmosphere reference condition and T is any temperature greater than T_1,

$$H_1 = Am_p q^*, \quad (2)$$

and

$$H = Am_{\mathrm{p}}[q^* + C_{\mathrm{v}}(T - T_{\mathrm{l}})], \tag{3}$$

where

$$q^* = q_{\mathrm{f}} + q_{\mathrm{v}} + q_{\mathrm{d}} \tag{4}$$

contains the energies of fusion and vaporization and the dissociation energies of the sub-electronvolt bonds in the molecule. A is the species average atomic mass, m_{p} is the proton mass, and C_{v} is the specific heat at constant volume. The absorbed laser intensity αI is expended in six processes listed in (5):

$$\begin{aligned}\alpha I = {} & \varrho v_{\mathrm{E}}\left[q^* + C_{\mathrm{p}}(T - T_{\mathrm{l}}) + v_{\mathrm{E}}^2/2\right] \\ & + x_{\mathrm{h}}\varrho_{\mathrm{s}}C_{\mathrm{v}}(T_{\mathrm{l}} - T_{\mathrm{o}})/\tau \\ & + \varepsilon\sigma_{\mathrm{SB}}T^4 + K(T - T_{\mathrm{o}})/x_{\mathrm{h}}.\end{aligned} \tag{5}$$

In (5),

$$x_{\mathrm{h}} = x_{\mathrm{o}} = x_{\mathrm{th}} - x_{\mathrm{v}} + 1/\alpha \qquad \text{if } x_{\mathrm{o}} > 0 \tag{6}$$

or

$$x_{\mathrm{h}} = \lambda \qquad \text{if } x_{\mathrm{o}} < 0 \tag{7}$$

and x_{h} is the thickness of the actual heated region during the laser pulse.

Taking the six terms in (5) in order, these energy sinks are (1) providing the energy q^* to a create a vapor of diatomic and atomic species, (2) further heating the vapor after it leaves the surface, (3) accelerating the vapor, (4) heating a chunk of surface of thickness x_{h} to temperature T_{l} from room temperature T_{o}, (5) black-body emission with emissivity ε from the half-plane facing the laser, and (6) conduction through the thermal gradient.

In (5), the exhaust velocity v_{E} is taken equal to the sound speed close to the target,

$$v_{\mathrm{E}} = c_{\mathrm{s}} = \sqrt{\frac{\gamma kT}{Am_{\mathrm{p}}}}, \tag{8}$$

and

$$\varrho = Anm_{\mathrm{p}} = \frac{Am_{\mathrm{p}}p}{kT} \tag{9}$$

is the vapor mass density.

2.2 *Fully ionized plasma regime*

Plasma absorbs laser radiation via inverse bremsstrahlung, i.e. absorption due to inelastic scattering of photons by free electrons, and becomes more dense until the 'critical density'

$$n_{\mathrm{ec}} = m_{\mathrm{e}}n^2\omega^2/4\pi e^2 = 1.115 \times 10^{21}/\lambda_{\mu\mathrm{m}}^2 \qquad \mathrm{cm}^{-3} \tag{10}$$

is reached, where $\lambda_{\mu\mathrm{m}}$ indicates the laser wavelength in μm. It can be shown that the effective thickness of the absorption zone is about $1/\alpha_{\mathrm{IB}}$, where α_{IB} is the inverse bremsstrahlung absorption coefficient:

$$\alpha_{\mathrm{IB}} \cong (\nu_{\mathrm{ei}}/c)(n_{\mathrm{e}}/n_{\mathrm{ec}}). \tag{11}$$

Surface plasma formation provides very high absorption. In local thermodynamic equilibrium [9], in the limit $\nu_{\mathrm{ei}}/\omega \ll 1$, and with $n \approx 1$ (valid for vacuum propagation), we have the familiar formula for the laser absorption depth:

$$\begin{aligned}x_\alpha = \frac{1}{\alpha_{\mathrm{IB}}} &= \left(\frac{\nu_{\mathrm{ei}}}{c}\frac{n_{\mathrm{e}}}{n_{\mathrm{ec}}}\right)^{-1} \\ &= \frac{2^{5/2}c\sqrt{m_{\mathrm{e}}}k^{3/2}n_{\mathrm{ec}}T_{\mathrm{e}}^{3/2}}{\pi^{3/2}Ze^4n_{\mathrm{e}}^2\ln\Lambda} = b\frac{n_{\mathrm{ec}}T_{\mathrm{e}}^{3/2}}{n_{\mathrm{e}}^2},\end{aligned} \tag{12}$$

which decreases with the square of the wavelength and is much smaller than the optical absorption depth in room-temperature transparent materials; it is more like that in metals. The equivalent thickness of the absorption zone can be as small as a wavelength of the incident laser light. For example, at the KrF laser wavelength, 2 eV plasma temperature, and $n_{\mathrm{e}} = 0.2n_{\mathrm{ec}} = 3.3 \times 10^{21}\ /\mathrm{cm}^3$, we find $1/\alpha = \lambda = 248$ nm.

The second process that occurs due to the mediation of plasma absorption at the target surface is UV conversion: much or even most of the light actually reaching the surface is UV with a peak radiation wavelength

$$\lambda_{\max} = 0.250/T_{\mathrm{e(ev)}} \qquad \mu\mathrm{m}. \tag{13}$$

Since plasma electron temperatures are often several eV, this is hard UV.

Our theoretical model [8] for determining surface pressure, electron temperature, coupling coefficient, and mass ablation rate in the vacuum-plasma regime is now widely accepted.

Using this model, C_{m} for essentially all 'surface-absorbing' materials in vacuum irradiated by pulsed lasers at any of the usual wavelengths, at or above plasma threshold intensity, can be estimated to within a factor of 1.5 from the expression ($\Psi = (A/2)[Z^2/(Z+1)]^{-1/3}$):

$$C_{\mathrm{m}} = 5.83 \times \frac{\Psi^{9/16}/A^{1/8}}{\left(I\lambda\sqrt{\tau}\right)^{1/4}} \qquad \mathrm{dyn/W}. \tag{14}$$

In addition, many transparent materials obey the same model when the intensity is high enough to form a surface plasma at the beginning of the pulse.

The only significant effort involved in interpreting this deceptively simple formula is that in determining the average ionization state Z of the ablation ejecta, which is done using the Saha equation [8].

Other results for electron temperature, density, and velocity near the absorber surface are shown in (15)–(17) (I_{sp} is velocity divided by the accelerator of gravity):

$$T_{\mathrm{e}} = 2.98 \times 10^4 \frac{A^{1/8}Z^{3/4}\left(I\lambda\sqrt{\tau}\right)^{1/2}}{(Z+1)^{5/8}} \qquad \mathrm{K}, \tag{15}$$

$$n_{\mathrm{e}} = 3.59 \times 10^{11} \frac{A^{5/16}I^{1/4}}{Z^{1/8}(Z+1)^{9/16}\tau^{3/8}\lambda^{3/4}} \qquad \mathrm{cm}^{-3}, \tag{16}$$

and

$$I_{sp} = 1.4 \times 10^3 \frac{A^{1/8}}{\Psi^{9/16}} \left(I\lambda\sqrt{\tau}\right)^{1/4}. \quad (17)$$

These relationships work well providing that the fluence exceeds the threshold for plasma formation $\Phi > \Phi_{plas}$. Otherwise, the C_m relationship breaks down as $\Phi \to 0$. The thermodynamics of plasma formation on a plane surface indicates that the fluence for plasma formation should be $\Phi_{plas} = F\tau^{0.5}$. Literature data can be combined to determine a best-fit expression [2]:

$$\Phi_{plas} = F\tau^m \qquad \mathrm{J/cm^2}, \quad (18)$$

with $F = 2.36 \times 10^4$ and $m = 0.45$.

2.3 *Code*

The photonic associates 'Clausius' code was developed specifically to take materials smoothly through the vapor regime into the plasma regime, using the relationships in Sects. 2.1 and 2.2, and computing the surface pressure for each pulsed laser intensity. The code begins iterating at room temperature, increasing T until (1) and (5) are balanced, and outputting the corresponding kinetic pressure p_{kin} and intensity I. This intensity drives a plasma-regime routine which computes the plasma ablation pressure $p = C_m I$ from (14) and, if $p_{plas} > p_{kin}$ or $I > I_{plas}$ (determined using (18)), switches to the plasma-regime model for final output. To treat compounds, the code iterates to produce a data point for each atomic species and then averages the results using weighting constants appropriate to the molecule (e.g. for a CH_2 monomer, C : 0.86, H : 0.14). Tabulated ionization energies up to XIII, and related partition functions for each atomic species, are incorporated [10].

Inputs are laser wavelength, material composition, heat of fusion, heat of vaporization, dissociation energy if appropriate, specific heat at constant volume, thermal conductivity, solid density, temperature for 1 atm vapor pressure, laser repetition rate, pulse number, pulse duration, and incident fluence.

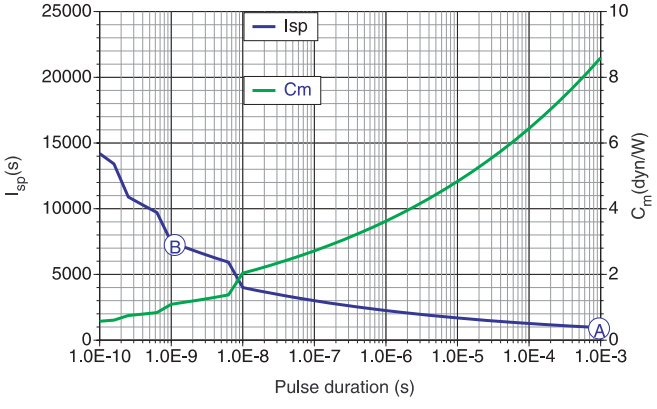

FIGURE 1 Predicted behavior of I_{sp} vs. pulse width τ for an aluminum target with a 200-mJ laser pulse incident at 1.06-μm wavelength and a fluence of 2.5 kJ/cm^2. (A) Where we are operating with our microthruster and (B) with 1-ns pulse duration

Outputs of the code are C_m, I_{sp}, q^*, average charge state Z, electron temperature T_e, atom temperature T, surface-recession velocity v_{rec}, ablation depth x_v, vapor velocity v, vapor mass density ϱ, and several diagnostics. No attempt is made to handle greater than one-dimensional expansions.

Figure 1 shows predictions for C_m and I_{sp} vs. pulse duration based on the surface-absorber theory. The figure shows that ns-duration pulses with quite low energy can still make available I_{sp} values as large as 8000 s, in good agreement with reported measurements [5].

3 Shadowgraphy

In order to learn more about the ablation process for possible photopolymer targets for the microthruster at nanosecond time scales, we carried out a time-resolved study of the plume using classical shadowgraphy. A dye cell was used as back illumination. The dye was pumped at 308 nm (XeCl laser, Lambda Physik Compex 205) for 532- and 1064-nm irradiation of the polymers, at 6 ns FWHM. The dye acted as a flashlight, with flashes in the range of 7 ns, while a CMOS camera with a zoom objective and open shutter times in the microsecond range was used. The two lasers (irradiation of the polymer and pumping of the dye cell) were synchronized by a delay generator which allowed us to record time-resolved shadowgraphy. As pump laser a Nd:YAG laser (6 ns, Quantel Brilliant B) was applied.

In this paper, we report ablation at fluences below the threshold for plasma creation.

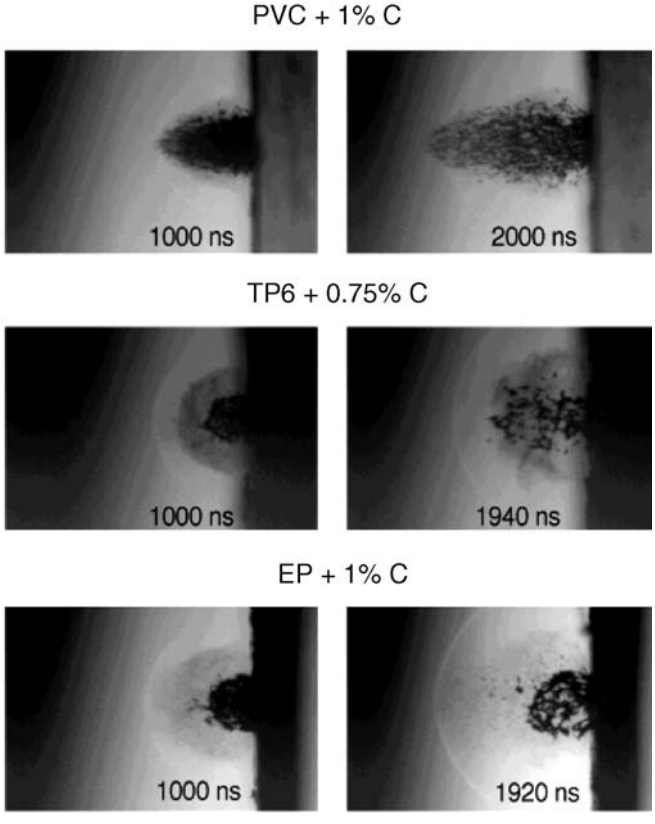

FIGURE 2 Comparison of shadowgraphy images for three polymers (1064-nm irradiation, 6-ns pulses). Fluence *from top*: 3.64, 5.44, and 6.47 J/cm^2

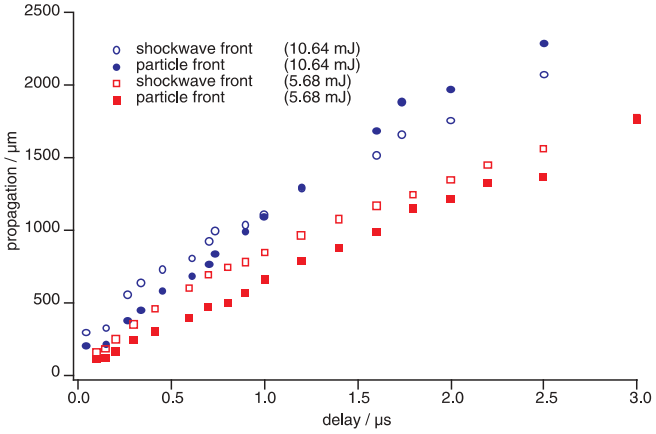

FIGURE 3 Analysis of the shock-wave and particle-front propagation for PVC doped with 1% of carbon. Irradiation at 1064 nm, using 6-ns duration pulses, with 3.64 J/cm^2 (10.64 mJ) and 1.94 J/cm^2 (5.68 mJ)

The images of the PVC ablation showed a very interesting behavior. The product ejection was more directional, resulting in an overtaking of the shock-wave (after 2 µs) front by the products (to our knowledge not observed before). This effect is only observed for higher irradiation fluences (e.g. not observed for a fluence of 1.94 J/cm^2) and only for PVC doped with carbon and an irradiation wavelength of 1064 nm. The reason for this behavior is not clear at present, but may be related to a large amount of solid products that are ejected during 1064-nm irradiation of PVC. The amount of solid fragments is higher for PVC compared to the triazene polymer (TP) and our proprietary exothermic polymer (EP), as shown in Fig. 2.

The images (after 1 and $\approx$ 2 µs) revealed that in the case of PVC a large amount of particles was ejected, with a bullet-like directional shape of the ablation products. For the irradiation of TP and EP, a quite different behavior was observed, i.e. the ablation products seemed to consist of two fractions: one with smaller fragments or maybe mainly gaseous products, and a second fraction with larger fragments. The shape of the ablation products was more hemispherical and with a slight mushroom form in the later stages (especially for TP). These shapes are consistent with the normally observed shapes during ablation. Other parameters that may influence the ablation characteristics will be discussed below.

The clear difference between the larger fragments and the gaseous products and the relatively sharp contours of the products allows analyzing the shadowgraphy pictures in more detail. Increasing laser fluence increases the shock-wave velocities. The analysis of the particle-front and shock-wave expansion is shown for PVC in Fig. 3 for two fluences (10.64 mJ corresponds to 3.64 J/cm^2, while 5.68 mJ corresponds to 1.94 J/cm^2). For the higher fluence it is clearly visible that the particle front overtakes the shock wave around 1 µs, while at the lower fluence the particle front may only reach the shock wave after 3 µs.

4 Comparison of theory and experiment

Table 2 illustrates the very large values of I_{sp} which have been obtained in the laboratory, and also indicates the degree to which our code gives results for a variety of materials which agree with observations.

Material	I (GW/cm^2)	τ (ns)	λ (nm)	Predicted I_{sp} (s)	Observed I_{sp} (s)	Reference
PVC	0.61	6	1064	960	640	This work
Al	450	7.5	0.694	9850	16 000	11
C	350	7.5	0.694	9450	19 000	11
$C_{16}H_{14}O_3$	4.0×10^6	0.30	1.32	2.0×10^5	4.0×10^5	12

TABLE 2 Comparison of theoretical predictions and literature data

We note that the particle-front and shock-wave velocities shown in Fig. 3 at 1 µs, for fluences below the plasma threshold, are about 1.15 km/s, but we see about 6.3 km/s for the first data point at 45 ns. This latter value corresponds to an I_{sp} of about 640 s. The laser–surface interactions reported here were done in air rather than vacuum, so that this very first data point is the only one relevant for matching a model for vacuum laser interaction. Indeed, the 'snowplow effect' of ambient air is expected to give a slightly lower result even for this early time than would be found in vacuum, and this is what we observe.

Data for the much higher I_{sp} values obtained in the plasma regime will be reported later, including plasma temperatures.

For the other comparison data in Table 2, we have chosen the classic first measurements of laser-driven ion velocities in the literature. In the first place, these examples illustrate the heroic I_{sp} values which can be obtained at ultra-high intensity. At more moderate intensities in the range that we plan for the advanced ns-pulse micro-laser plasma thruster (µLPT), the examples in Table 2 show I_{sp} values at the high end of the range shown in Fig. 1. In these cases, our model predicts I_{sp} to within a factor of two, and errs by underestimating this parameter.

5 Conclusions

Present status and performance of the existing, ms-pulse µLPT have been discussed and compared with performance advantages which we expect to achieve with ns-pulse duration. Our code predictions, as well as reported measurements [5], indicate that we will be able to access the range from moderate to very high values of I_{sp} by using ns pulses at appropriate fluences.

ACKNOWLEDGEMENTS This work was completed with support from AFOSR Contract No. F49620-00-C-0005 by the Swiss National Science Foundation, and is also based in part upon work supported by the European Office of Aerospace Research and Development, Air Force Office of Scientific Research, Air Force Laboratory, under Contract No. F61775-01-WE057. Additional support was provided by Photonic Associates' Internal Research and Development Fund.

REFERENCES

1 C. Phipps, J. Luke, G. McDuff, T. Lippert: Appl. Phys. **77**, 193 (2003)
2 C. Phipps, J. Luke: AIAA J. **40**, 310 (2002)
3 C.R. Phipps, J. Luke: 'Micro Laser Plasma Thrusters for Small Satellites'. In: *Proc. High Power Laser Ablation Conf., Santa Fe, NM, 2000* [SPIE **4065**, 801 (2000)]
4 C.R. Phipps, J. Luke, J. Marquis: 'Diode Laser-based Microthrusters: a New Alternative for High I_{sp}, Long-life Engines'. In: *36th AIAA/ASME/SAE/ASEE Joint Propulsion Conf., Huntsville, AL, 2000*
5 C. Phipps, M. Michaelis: J. Laser Particle Beams **12**, 23 (1994)

6 F. di Teodoro, J. Koplow, S. Moore: Opt. Lett. **27**, 518 (2002)
7 D. Gonzales, R. Baker: 'Microchip Laser Propulsion for Small Satellites'. In: *37th AIAA/ASME/SAE/ASEE Joint Propulsion Conf., Salt Lake City, UT, 2001*
8 C.R. Phipps, Jr., T.P. Turner, R.F. Harrison, G.W. York, W.Z. Osborne, G.K. Anderson, X.F. Corlis, L.C. Haynes, H.S. Steele, K.C. Spicochi, T.R. King: J. Appl. Phys. **64**, 1083 (1988)
9 R.E. Kidder: *Proc. International School of Physics, Course 48*, ed. by P. Caldirola, H. Knoepfel (Academic, New York 1971)
10 C.W. Allen: *Astrophysical Quantities* (Athlone, London 1973) pp. 33–40
11 D.W. Gregg, S.J. Thomas: J. Appl. Phys. **37**, 4313 (1966)
12 K. Eidmann, F. Amiranoff, R. Fedosejevs, A.G.M. Maaswinkel, R. Petsch, R. Sigel, G. Spindler, Y. Teng, G. Tsakiris, S. Witkowski: Phys. Rev. A **30**, 2568 (1984)